RSC Advances

PAPER

View Article Online
View Journal | View Issue

Cite this: *RSC Adv.*, 2023, **13**, 14018

Optimizing the performance of $Au_y/Ni_x/TiO_2$NTs photoanodes for photoelectrochemical water splitting†

Shaimaa K. Mohamed, *[a] Amany M. A. Bashat,[a] Hassan M. A. Hassan, *[a] Nahla Ismail[b] and Waleed M. A. El Rouby *[c]

Water splitting using photoelectrochemical (PEC) techniques is thought to be a potential method for creating green hydrogen as a sustainable energy source. How to create extremely effective electrode materials is a pressing concern in this area. In this work, a series of Ni_x/TiO_2 anodized nanotubes (NTs) and $Au_y/Ni_x/TiO_2$NTs photoanodes were prepared by electrodeposition *via* cyclic voltammetry and UV-photoreduction, respectively. The photoanodes were characterized by several structural, morphological, and optical techniques and their performance in PEC water-splitting for oxygen evolution reaction (OER) under simulated solar light was investigated. The obtained results revealed the nanotubular structure of TiO_2NTs was preserved after deposition of NiO and Au nanoparticles while the band gap energy was reduced allowing for effective utilization of solar light with lower charge recombination rate. The PEC performance was monitored and it was found that the photocurrent densities of Ni_{20}/TiO_2NTs and $Au_{30}/Ni_{20}/TiO_2$NTs were 1.75-fold and 3.25-fold that of pristine TiO_2NTs, respectively. It was confirmed that the performance of the photoanodes depends on the number of electrodeposition cycles and duration of photoreduction of gold salt solution. The observed enhanced OER activity of $Au_{30}/Ni_{20}/TiO_2$NTs could be attributed to the synergism between the local surface plasmon resonance (LSPR) effect of nanometric gold which increased solar light harvesting and the p–n heterojunction formed at the NiO/TiO_2 interface which led to better charge separation and transportation suggesting its potential application as an efficient and stable photoanode in PEC water splitting for H_2 production.

Received 27th March 2023
Accepted 2nd May 2023

DOI: 10.1039/d3ra02011h

rsc.li/rsc-advances

1. Introduction

Developing renewable, sustainable, and clean energy resources continues to be at the core of scientific research nowadays to address the growing problems of energy demand and environmental pollution.[1–4] One of the most promising green strategies is utilization of solar energy in the production of hydrogen gas by PEC water splitting as it can store the renewable and clean solar energy in chemical bonds while operating at low input bias and room temperature.[1,4,5] In addition, hydrogen is considered an ideal energy carrier due to its renewability, cleanliness, high energy density and zero CO_2 emissions.[6–9] The efficiency of PEC water splitting is greatly dependent on the following crucial factors: (i) efficient utilization of solar energy *via* minimizing the band gap of the semiconductor photoelectrode; (ii) the charge transfer rate to the photoelectrode/electrolyte interface and (iii) rapid surface reaction between the photogenerated electrons/holes and the electrolyte.[10] Current research is focusing on enhancing the efficiency of the process through controlling the photoelectrode morphology, tuning the band gap, optimizing electrolyte conditions, and engineering of designed interfaces.[11,12]

One of the most employed photoanodes is TiO_2 nanotube arrays (TiO_2NTs) which stands out other titania structures due to stability, highly oriented electron transportation channels and its larger surface area resulting in enhanced diffusion of light, photogenerated carriers and reactants through the entire tubular depth.[13,14] However, large bandgap implying weak solar light absorption and high carrier recombination rates are major drawbacks which can be overcome by chemical modification in the design of the photoanode material.[15] The modification strategies may be directed to band gap reduction *via* chemical doping,[16] retardation of charge recombination by heterojunction formation with other materials[17,18] and enhancing solar energy harvesting through surface sensitization.[19–21]

It is widely acknowledged that doping of transition metal ions can help reducing the band gap thereby extended solar energy

[a]*Department of Chemistry, Faculty of Science, Suez University, 43518, Suez, Egypt. E-mail: Shaimaa.Mohamed@Sci.suezuni.edu.eg; h.hassan@suezuniv.edu.eg*

[b]*Physical Chemistry Department, Centre of Excellence for Advanced Sciences, Renewable Energy Group, National Research Centre, Dokki, 12311, Giza, Egypt*

[c]*Materials Science and Nanotechnology Department, Faculty of Postgraduate Studies for Advanced Science (PSAS), Beni-Suef University, 62511 Beni-Suef, Egypt. E-mail: waleedmohamedali@psas.bsu.edu.eg*

† Electronic supplementary information (ESI) available. See DOI: https://doi.org/10.1039/d3ra02011h

absorption to the visible range while acting as a trap for the photogenerated electrons thus suppressing the carrier recombination rate.[22–24] Ni or Ni – related species (*i.e.* NiO, NiOOH, Ni–NiO) were reported to boost the photocatalytic activity of titania towards H_2 production with a relative uncertainty about the active reaction center (Ni^0 or Ni^{2+}).[25–32] Dong *et al.*[30] prepared Ni-doped TiO_2 nanotubes by anodizing Ti–Ni alloys and found that the photoconversion efficiency of PEC water splitting was enhanced 3.35 times the undoped titania which was attributed to improved light absorption and facilitated separation of photogenerated electron–hole pair. Li *et al.*[33] contributed the enhanced photocatalytic and photoelectrochemical activity of NiO/TiO_2 hollow microspheres to the construction of p–n junctions with an inner electric field between TiO_2 and NiO.

Localized surface plasmonic resonance effect of nanometric gold has been reported to enhance PEC water splitting *via* facilitating oxygen evolution reaction.[14,34] Through LSPR the interactions between irradiation photons and Au atoms are enhanced thus increasing visible light absorption on semiconductor surface and reducing diffusion distance of the photogenerated holes to the electrode/electrolyte interface.[34]

Improvement of PEC water-splitting performance can be expected by co-doping transition metal and plasmonic material like Au due to synergistic effects.[34] Oros-Ruiz *et al.*[35] found that Au–NiO/TiO_2–P25 photocatalyst prepared by deposition–precipitation method were superior to pristine titania in the photocatalytic water splitting reaction for hydrogen production. However, doping of TiO_2NTs with both NiO and Au and utilization of the prepared nanotubular photoanode in PEC water-splitting for H_2 production is seldom reported. In this work, highly ordered TiO_2NTs were synthesized by anodization method and a series of Ni_x/TiO_2NTs photoanodes were prepared through electrodeposition. Another series of Au_y/Ni_x/TiO_2NTs photoanodes were prepared by facile and simple photoreduction method. The performance of the prepared photoelectrodes was investigated in PEC water-splitting for H_2 production under simulated sun light.

2. Materials and methods

2.1 Materials

A titanium plate (99.9%) was purchased from AMERICAN ELEMENTS (USA). Ammonium fluoride (95%) and nickel chloride (98%) were purchased from Winlab laboratory chemicals reagents fine chemicals (United Kingdom). Gold(III) chloride trihydrate ($HAuCl_4 \cdot 3H_2O$), acetone (≥99.8) and ethanol (≥99.5%) were purchased from (Sigma Aldrich, Germany). Trisodium citrate ($C_6H_5O_7Na_3 \cdot 2H_2O$) was purchased from (Qualikems, India). Ethylene glycol (99.9%) was obtained from (Pharmco Product Inc., North America). Sodium sulphate (Oxford Laboratory Reagents, India). All chemicals were utilized without further purification. All the solutions were prepared by deionized water.

2.2 Synthesis of the photoelectrodes

2.2.1 Fabrication of TiO_2NTs photoanode. TiO_2NTs were fabricated through anodization of titanium foil (2 × 1.5 cm). The titanium foils were ultrasonically cleaned with acetone, ethanol and deionized water for 30 min sequentially and dried in N_2 stream for 3 min. The anodization of the cleaned titanium foil was performed in a mixture of ethylene glycol, 0.3 wt% ammonium fluoride and 2 wt% deionized water at 40 V for 1 h. Then, the anodized Ti foil was ultra-sonicated with ethanol and annealed in air at temperature of 450 °C for 3 h with a heating rate of 5 °C min^{-1}.

2.2.2 Fabrication of Ni_x/TiO_2NTs photoanodes. The prepared TiO_2NTs was dipped in 50 mL of 0.05 M $NiCl_2$ electrolyte solution in a conventional electrochemical cell with a three-electrode system, containing a platinum electrode as the counter electrode and an Ag/AgCl electrode as the reference electrode. The cyclic voltammetry method was utilized in the negative potential range of −0.1 to −0.5 V at scanning rate 10 mV s^{-1} to obtain the Ni_x/TiO_2 NTs photoanodes at different number of cycles (where x represents the number of cycles = 3, 5, 10, 20 or 30). The prepared photoelectrodes were dried at 80 °C for 2 h and annealed in air at temperature of 450 °C for 3 h with a heating rate of 5 °C min^{-1} to obtain the NiO phase.

2.2.3 Fabrication of (Au_y/Ni_{20}/TiO_2NTs) photoanodes. The photoelectrode Ni_{20}/TiO_2NTs was selected to continue the fabrication process based on its performance in the PEC water-splitting reaction. A series of Au_y/Ni_{20}/TiO_2 NTs photoelectrodes were prepared by photoreduction under UV irradiation (where y represents irradiation duration = 15, 30, 60 or 120 min). Unannealed Ni_{20}/TiO_2 NTs was immersed in solution of 0.05 mM $HAuCl_4$ and 1 mM tri-sodium citrate which act as capping and reducing agent and was irradiated with UV light (λ = 365 nm) for different durations. After washing with deionized water, the product was calcined in air at temperature of 450 °C for 2 h with a heating rate of 2 °C min^{-1}. The fabrication process scheme is summarized in Fig. 1.

2.3 Characterization of the prepared materials

A field emission scanning electron microscope (FE-SEM, ZEISS Sigma 500VP) was used for checking the surface morphologies of the different samples. Elemental analysis was performed by energy-dispersive X-ray spectroscopy (EDS) analysis using equipment fixed on the SEM and operated with an acceleration voltage of 15 kV. High-resolution transmission electron microscope (HRTEM) images were taken by JEOL JEM-2100 electron microscope, where sample was prepared for analysis by scratching from titanium substrate, then ultrasonicated with ethanol. X-ray diffraction (XRD) was performed using a (Bruker D8 Advance, Germany) X-ray powder diffractometer, using Cu Kα radiation (wavelength 1.54 A, 40 mA, 45 kV). The Shimadzu 2600 spectrophotometer, Japan with Ba_2SO_4 as the reflectance standard was used for UV-vis analysis. Photoluminescence (PL) spectra were measured using JASCO (FP-8300) spectrofluorometer.

2.4 Photoelectrochemical measurements

The photoelectrochemical measurements were performed by Biologic SP-150 potentiostat. The performance of the fabricated photoelectrodes in PEC water-splitting was investigated by its

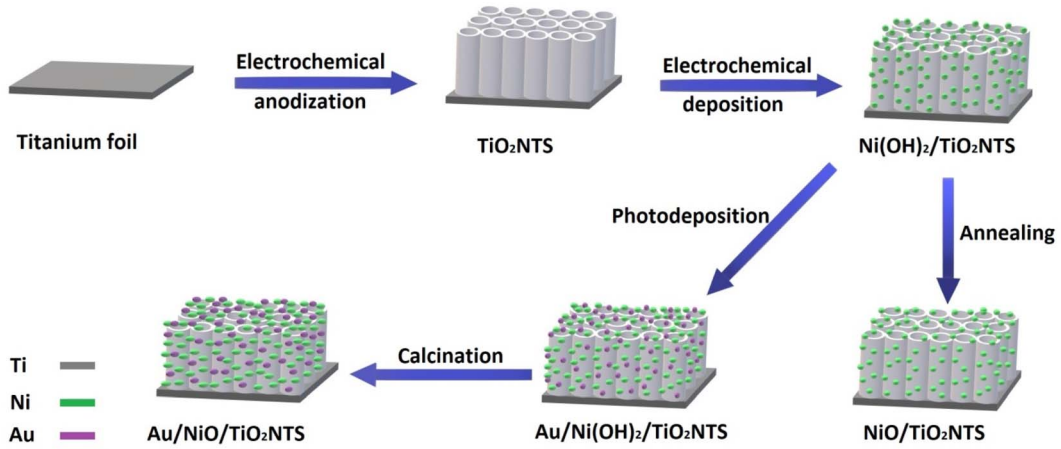

Fig. 1 Scheme of the procedure for the preparation of Ni_x/TiO_2NTs and $Au_y/Ni_x/TiO_2NTs$ photoanodes.

utilization as the working electrode (1.5 cm × 1 cm) in a three-electrode configuration cell with Pt electrode as a counter electrode and Ag/AgCl reference electrode where 0.5 M Na_2SO_4 solution (pH ~ 7) served as the electrolyte. The working photoelectrode was illuminated by xenon lamp-simulated solar light (100 mW, 1.5 AM). Three techniques were used to monitor the performance namely, liner sweep voltammogram (LSV), chronoamperometric measurements, and electrochemical impedance spectroscopy (EIS). Linear sweep voltammetry was measured in the voltage window starting from −0.6 V to +1 V at a scan rate of 10 mV s^{-1} and under chopped applied (ON/OFF) cycles with intervals of 5 s in the dark and 5 s under illumination. Chronoamperometry was performed under chopped applied ON/OFF cycles with intervals of 30 s in the dark and 30 s under illumination and the measurements were performed at 1 V *vs.* Ag/AgCl under continuous simulated sunlight illumination for 6 minutes. The electrochemical impedance spectroscopy measurements were measured for frequency range 0.05 Hz to 100 KHz at potential of 0 V *vs.* Ag/AgCl electrode with an amplitude of 10 mV. The stability of the fabricated photoelectrodes was measured by chronoamperometry at 1 V (*vs.* Ag/AgCl) for 1 h in 0.5 M Na_2SO_4 solution.

3. Results and discussion

3.1 Structural, chemical, optical and morphological characterization of $Au_y/Ni_x/TiO_2NTs$ photoelectrodes

The morphologies of the photoelectrodes are investigated by FESEM and are given in (Fig. 2–4). Fig. 2a and b present the top-view and cross-sectional FESEM images of TiO_2NTs photoelectrode, respectively, which demonstrate the nanotube array uniformity with average diameter around 70 nm, the wall thickness 20 nm and the tubes length ranging from 1.4–2.0 μm. The length of the prepared TiO_2NTs is favourable for the photoelectrocatalytic water splitting reaction because the maximum penetration depth of light in TiO_2 nanotubes is 2.0 μm, tubes longer than 2.0 is expected to show higher electronic resistance which would retard the photogenerated carriers transportation rate[36,37] and facilitate recombination of the photogenerated electron–hole pairs.[14]

Fig. 3a–e shows the Ni_x/TiO_2NTs photoelectrodes with NiO nanoparticles deposited onto the top and inner walls of TiO_2-NTs while the tubular morphology is preserved. The spacing among nanotubes is no longer obvious, and the nanotube inner diameter and wall become smaller and thicker due to the

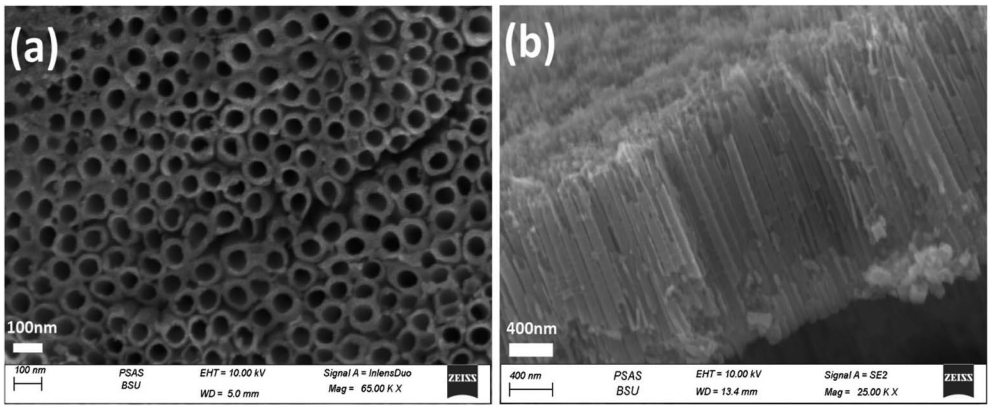

Fig. 2 Top-view (a) and side-view (b) FESEM images of TiO_2NTs photoanode.

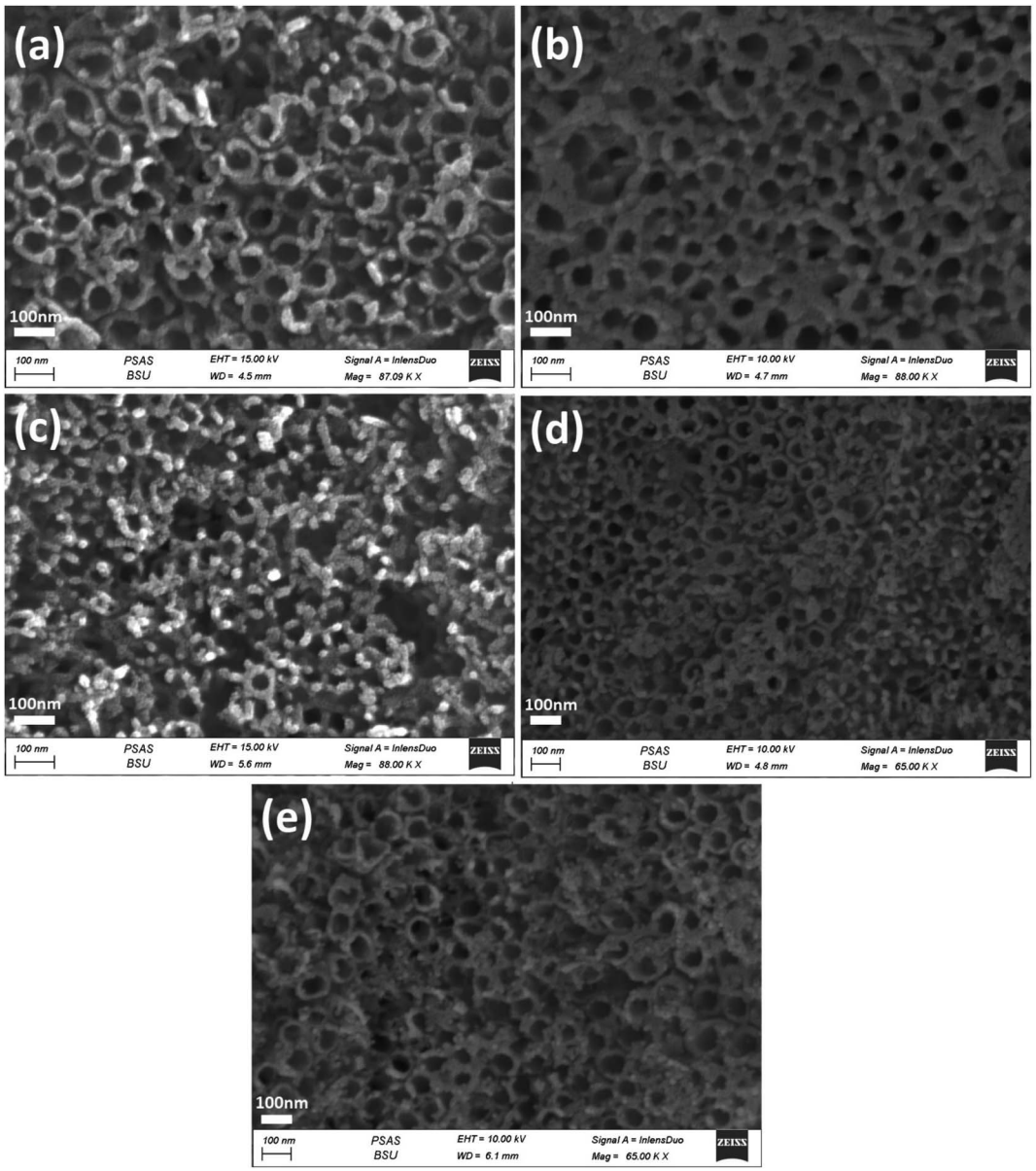

Fig. 3 FESEM images of the top-view of Ni_x/TiO_2NTs photoanodes synthesised by different electrodeposition cycles (a) 3 cycles, (b) 5 cycles, (c) 10 cycles, (d) 20 cycles and (e) 30 cycles.

deposition of Ni species on the outer and inner surfaces of the tubes. The Ni_x/TiO_2NTs photoelectrode prepared at 30 cycles showed clogged tubes due to increasing amount of deposited NiO nanoparticles. The morphology of $Au_y/Ni_{20}/TiO_2$NTs photoelectrodes was given by Fig. 4a–d. The images revealed that the photoreduction deposition of gold didn't change the morphology of tubes and a further clogging is observed with increasing the time intervals of reduction.

The energy dispersive X-rays' analysis was performed for all fabricated photoelectrodes (Fig. S1–S10†), and the calculated element's atomic percent were presented in Table 1. The presence of the elements Ti, Ni and Au is confirmed in a manner corresponding to the preparation method. The amount of Ni was raised gradually by increasing the number of cycles of electrodeposition from 5 to 20 cycle. It was found in photoelectrodes containing gold that the amount of Au increased as the time intervals of photoreduction deposition increased. The EDS elemental mapping results is present in Fig. 5 for one selected photoelectrode ($Au_{30}/Ni_{20}/TiO_2$NTs) where nickel (Ni), gold (Au) elements were uniformly and homogenously deposited on the surface of titania tubes. This would lead to well – dispersed active sites along the tubes which enhance the efficiency of the photoelectrocatalytic reaction.[38]

HRTEM images for one selected photoelectrode $Au_{30}/Ni_{20}/TiO_2$NTs showed in Fig. 6 confirmed the nano-tubular structure. The surface of TiO_2NTs was rough where gold (Au) and nickel (NiO) particles can be found dispersed all over the surface of nanotubes. The lattice fringes of 0.31 nm corresponds to the

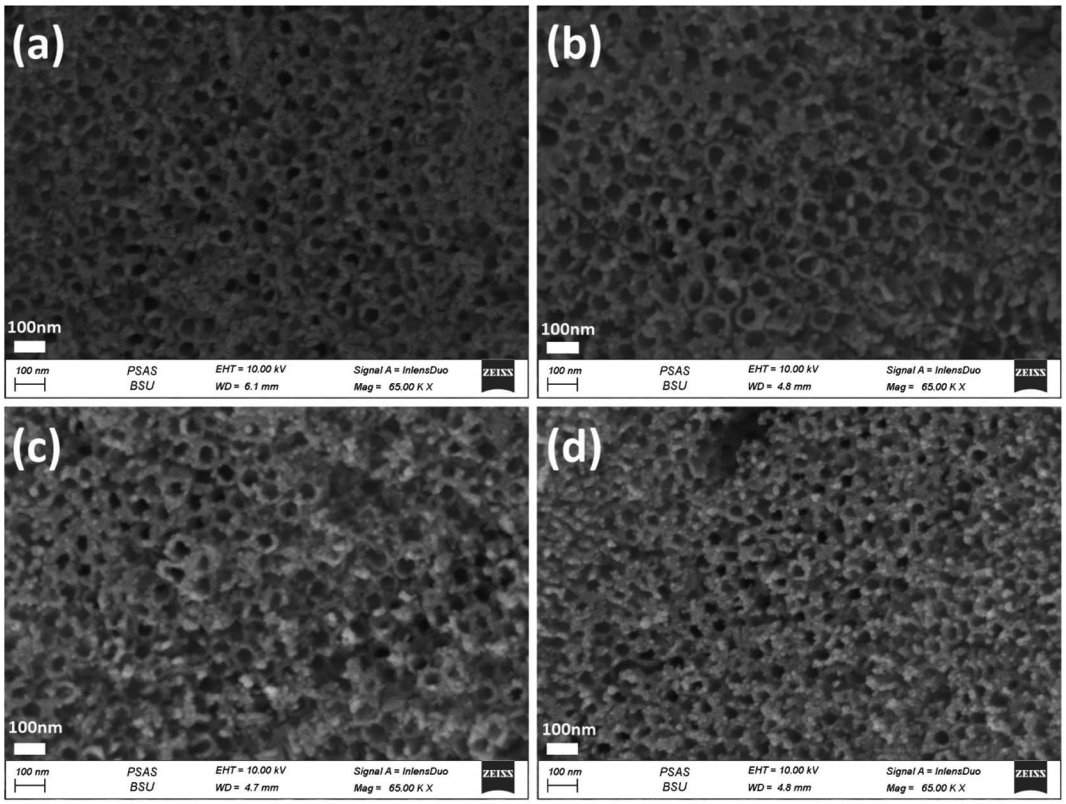

Fig. 4 FESEM images of the top-view of $Au_y/Ni_{20}/TiO_2NTs$ photoanodes synthesised by different time intervals of photodeposition (a) 15 min, (b) 30 min, (c) 60 min and (d) 120 min.

Table 1 Elemental composition and band gap values of the prepared photoanodes

Photoelectrode	Ti	O	Ni	Au	Band gap (eV)
TiO_2	14.70	85.30			3.05
Ni_3/TiO_2NTs	26.19	73.47	0.34		2.85
Ni_5/TiO_2NTs	26.15	73.47	0.38		2.83
Ni_{10}/TiO_2NTs	26.98	72.60	0.42		2.82
Ni_{20}/TiO_2NTs	29.84	69.70	0.46		2.80
Ni_{30}/TiO_2NTs	12.69	86.86	0.45		2.81
$Au_{15}/Ni_{20}/TiO_2NTs$	12.62	86.82	0.36	0.20	2.93
$Au_{30}/Ni_{20}/TiO_2NTs$	14.39	84.96	0.42	0.23	2.89
$Au_{60}/Ni_{20}/TiO_2NTs$	13.59	85.70	0.39	0.33	2.95
$Au_{120}/Ni_{20}/TiO_2NTs$	13.10	86.03	0.51	0.37	2.96

reflection from the (101) plane of anatase TiO_2 is identified as seen in Fig. 6b.[37] Fig. 6 c represented the selected area electron diffraction (SAED) which confirmed the crystalline structure of the photoelectrode and the presence of diffraction rings corresponding to (101), (103), (200), and (220) planes of TiO_2.[39] The (220) and (311) planes corresponded to metallic gold[40] where the plane (110) may be indexed to NiO phase.[41]

The XRD diffractograms of the prepared photoelectrodes were given in Fig. 7. All prepared samples showed the presence of three phases which are metallic titanium, anatase and rutile. The peaks corresponding to anatase appeared at $2\theta = 25.1°$, 37.7° and 48° characteristic of (101), (004) and (200) planes, respectively (JCPDS 21-1272).[19,42] The peaks at $2\theta = 38.2°$, 40°, 52.8°, 70.4° and 76.1° corresponded to (002), (101), (102), (103) and (112) planes, respectively of metallic titanium, (JCPDS 44-1294), attributed to the metallic substrate.[43] Small peaks due to rutile as a minor phase was located at $2\theta = 27.2°$, 35°, 53.85°, 55° and 68.8° characteristic of (110), (101), (200), (211), and (220) planes (JCDPDP 01-089-8304).[44] The anatase: rutile ratio was 2 : 1 in TiO_2NTs sample suggesting enhanced performance in PEC due to improved hole transfer rate across TiO_2NTs/electrolyte interface.[42,45] The crystalline size of the anatase phase was found to be 25 nm confirming the nanostructure of the prepared tubes. There were no peaks detected for gold or nickel phases may be due to its low concentration[42,46] and high dispersion. Another possible explanation may be provided by considering the limitations of X-ray powder diffraction technique.[47] Amorphous phases do not give rise to diffraction peaks. Phase overlap may hinder phase identification while due to matrix effects, strongly diffracting phases would obscure weakly diffracting one. Thus, any of the above-mentioned reasons may account for the absence of diffraction peaks for gold and nickel – containing phases.

Fig. 8 represents XPS spectra for $Au_{30}/Ni_{20}/TiO_2NTs$ photoelectrode which was analysed to determine surface chemical composition and oxidation states. Peaks at 459.4 and 465.1 eV of the titanium spectra corresponded to photoelectronic splitting of $2p_{1/2}$ and $2p_{3/2}$ Ti^{4+} orbitals.[48] The XPS spectra for Au 4f

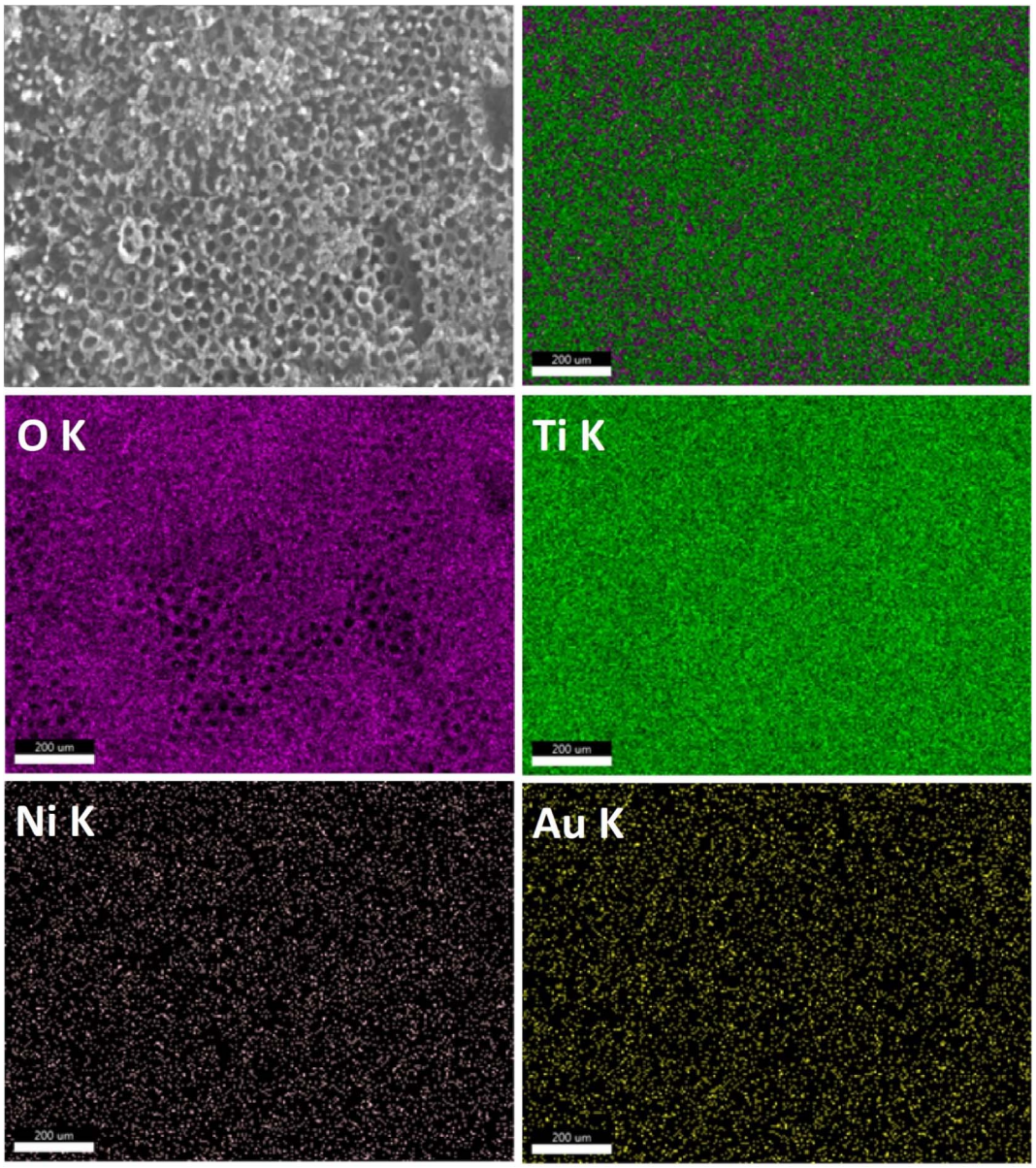

Fig. 5 The EDS elemental mapping of $Au_{30}/Ni_{20}/TiO_2NTs$.

showed two peaks at binding energies of 84.0 and 87.6 eV due to Au $4f_{7/2}$ and Au $4f_{5/2}$, respectively which confirmed the presence of Au^0.[49] The deconvoluted spectra of O 1s showed two peaks at 530.6 eV was attributed to the lattice oxygen of TiO_2 or the metal–oxygen bond[50] and 532.1 eV resulted from the existence of O–H bond.[51] The Ni 3p region was used to analyse the

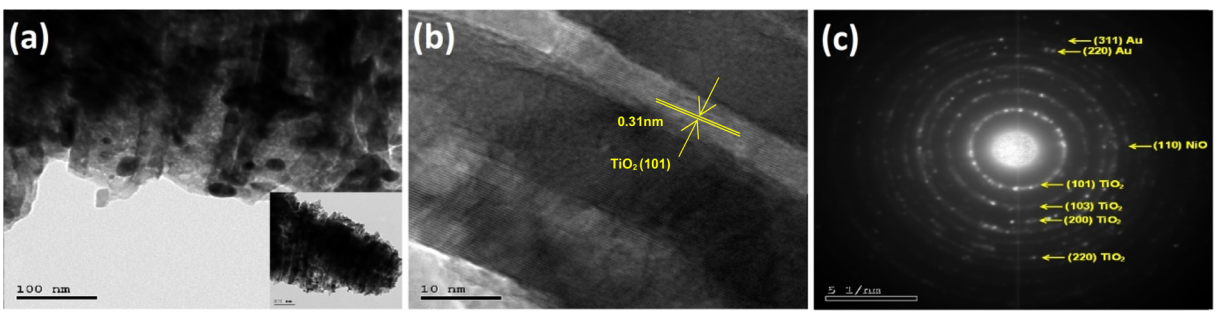

Fig. 6 (a and b) HRTEM images of $Au_{30}/Ni_{20}/TiO_2NTs$ and (c) SAED patterns of photoanode.

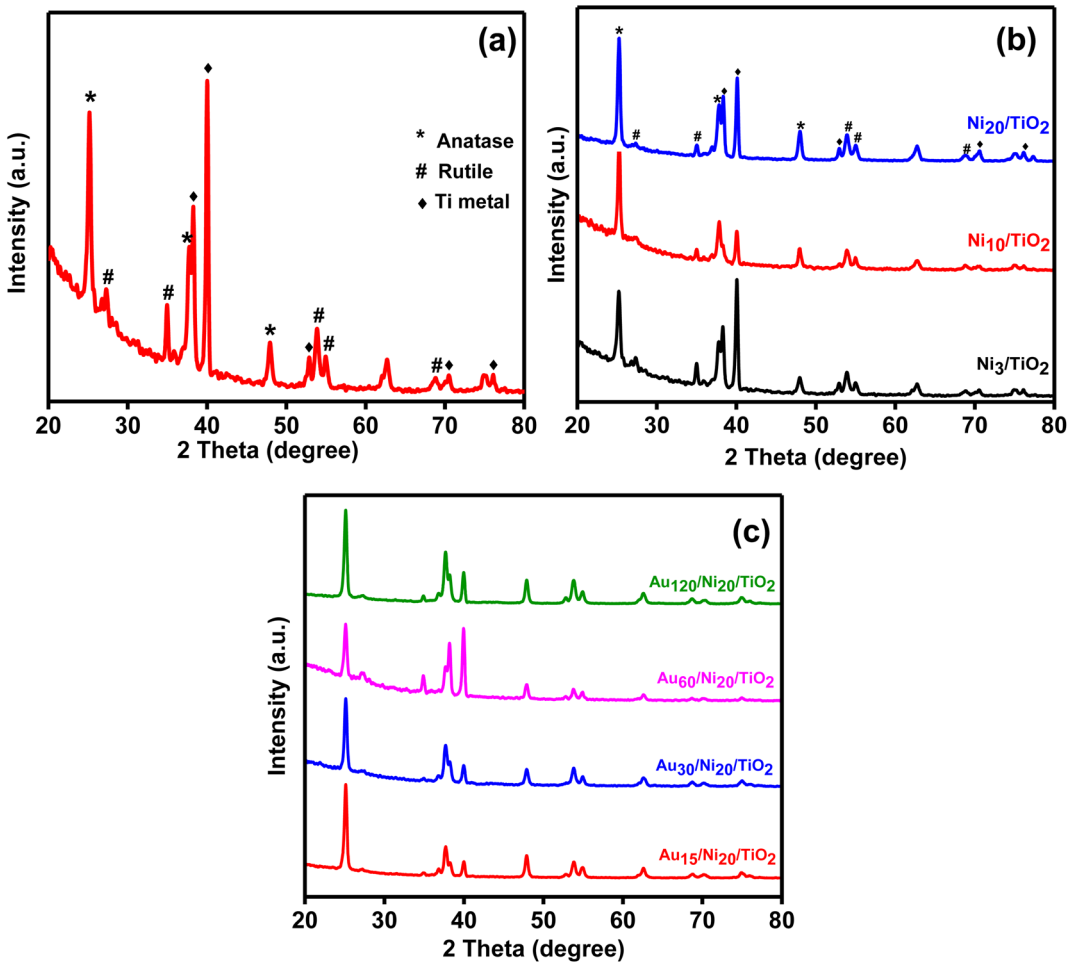

Fig. 7 XRD diffractograms for the prepared TiO_2NTs photoanode (a), Ni_x/TiO_2NTs photoanodes (b) and $Au_y/Ni_{20}/TiO_2$NTs photoanodes (c).

oxidation state of nickel in the prepared photoelectrode similar to Amaya-Dueñas *et al.*[52] and peak at 63.7 eV was observed and it was assigned to NiO.[53]

Fig. 9 depict the UV-vis diffuse reflectance absorption spectra (DRS) of the pure TiO_2NTs, Ni_x/TiO_2 and $Au_y/Ni_x/TiO_2$NTs photoelectrodes in the range of 200–600 nm. The strong absorption observed in a wavelength region below 403 nm for the pure TiO_2NTs is due to the intrinsic inter-band transition absorption of TiO_2NTs.[54,55] The light absorption edge was red shifted to the visible light for Ni_x/TiO_2NTs (Fig. 9a) photoelectrodes which can be explained by formation of a p–n heterojunction was formed across TiO_2/NiO interface leading to electron excitation by visible light photons. $Au_y/Ni_{20}/TiO_2$NTs (Fig. 9b) photoelectrodes showed enhanced absorption in the visible light region than pristine TiO_2NTs while absorption peak in the range of 500–600 nm appeared in the spectrum. This peak resulted from the LSPR effect induced by gold nanoparticle.[34,56,57] It has been reported that the LSPR effect leads to enhanced OER performance of photoanodes.[34,58] To estimate the band gap energy of the prepared photoelectrodes, Kubelka–Munk transformation on the obtained UV-vis absorption data was used to produce Tauc plot which was represented by Fig. 9c and d. A Tauc plot was constructed by plotting $(\alpha h\nu)^{1/2}$ *versus* $h\nu$ and the band gap energy (E_g) values were obtained by extrapolating linear region of the curves to meet *x*-axis[59] and cited in Table 1. The E_g value of TiO_2NTs was found to be 3.05 eV in accordance with the reported data of titania nanotubes.[60] TiO_2NTs band gap is due to Ti 3d and O 2p hybridized states where the conduction band's lowest edge being formed by Ti d_{xy} states and the O $2p_xp_y$ states forms the highest edge of valence band.[14] Ni_x/TiO_2NTs and $Au_y/Ni_{20}/TiO_2$NTs showed a narrowed band gap suggesting photoinduction of e^-/h^+ pair by visible light thus maximizing utilization of solar light. The obtained results are in accordance with Oros-Ruiz *et al.* who reported reduction of band gap value of TiO_2–P25 from 3.1 to 2.9 eV after loading of Au–NiO.[35]

Photoluminescence (PL) spectra of the prepared photoelectrodes were investigated to study surface processes including photoexcited e^-/h^+ recombination rate and the efficiency of charge trapping and given in Fig. 10. The PL spectra of TiO_2NTs showed the highest intensity and exhibited peaks at 420 and 452 nm assigned to self-trapped excitons[61] where peaks at 469, 482 and 502 nm can be ascribed to oxygen vacancies and surface defects.[62] The PL spectra of Ni_x/TiO_2NTs photoelectrodes showed the same peaks but with reduced intensity indicating lower rate of photoexcited e^-/h^+ recombination and

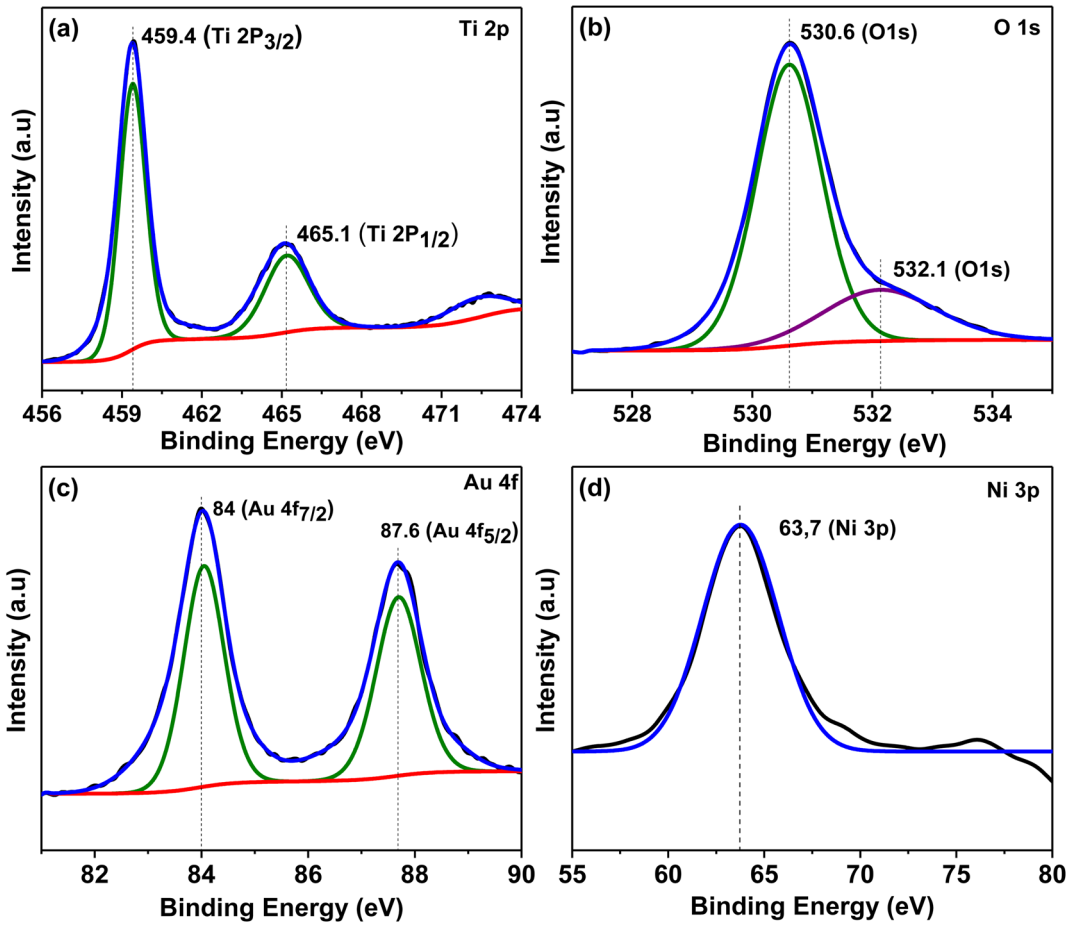

Fig. 8 XPS spectra for $Au_{30}/Ni_{20}/TiO_2NTs$ photoelectrode (a) Ti 2p, (b) O 1s, (c) Au 4f and (d) Ni 3p.

improved efficiency of charge separation which is beneficial in the PEC process.[43] Further reduction in the intensity was observed in $Au_y/Ni_{20}/TiO_2NTs$ photoelectrodes due to emerging trapping sites resulted from Au doping. The intensities of PL peaks of Ni_x/TiO_2NTs and $Au_y/Ni_{20}/TiO_2NTs$ samples were generally lower than pristine titania nanotubes. The PL intensities of $Au_y/Ni_{20}/TiO_2NTs$ were decreased in the order $Au_{120} \approx Au_{60} > Au_{30} \approx Au_{15}$. It is known that PL signals of semiconductor materials result from the recombination of photoinduced charge carriers thus in general, the lower the PL intensity, the lower the recombination rate of photoinduced electron–hole pairs, and hence higher photocatalytic activity.[63] However, the PL mechanisms of semiconductor nanoparticles are very complex, and it is not possible to extrapolate the contribution of the single factors since various parameters, as for instance particle size, recombination velocity, and presence of defects, are responsible in a different way for the shape and intensity of PL spectra. In this work, different periods were used for photo deposition of Au which might affected the particle size of Au giving rise to larger size at extended deposition duration. This could affect the rate of carriers' recombination and hence the PL intensity. Same behavior was reported by Khore *et al.*[49] where the PL intensities of $Au@TiO_2$ composites were decreased by increasing Au loading to 2% then increased when the loading reached 3% Au. Also, Lin *et al.*[64] reported the intensity of the PL emission signals decreased with the decreasing of the Au NPs sizes indicating the radiation recombination of the photo-induced carriers were suppressed when the Au NPs became smaller.

3.2 Photoelectrochemical performance of the prepared photoelectrodes

Linear sweep voltammetry measurement (Fig. 11) illustrated that TiO_2NTs, Ni_x/TiO_2NTs and $Au_y/Ni_{20}/TiO_2NTs$ photoelectrodes are all n-type semiconductors and exhibited an OER activity since under light irradiation, the photocurrent increases when the applied anodic potential is increased.[65] TiO_2NTs showed the lowest photocurrent density of 0.08 mA cm^{-2} attributed to the wide band gap (3.05 eV) and higher rate of recombination of photogenerated charge carriers.[27] Ni_x/TiO_2-NTs photoanodes (Fig. 11a) exhibited higher water photooxidation activities and higher photocurrent densities than TiO_2NTs. This behavior is attributed to efficient separation of photogenerated charge carriers due to the Ni 3d states serving as trapping sites for photogenerated electrons from the VB which is in accordance with the PL results. The same enhancement in behavior was also reported for Ni doped titania photoanodes in PEC water splitting by many groups.[26–28,30,66] The

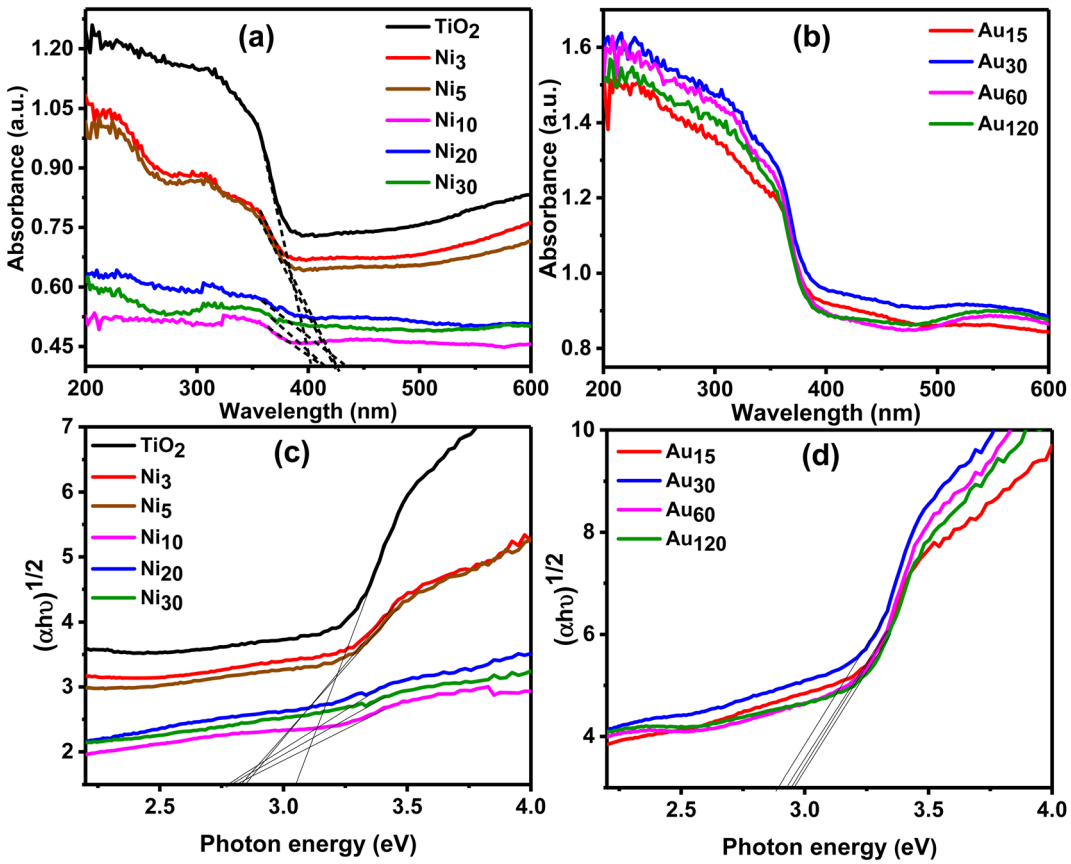

Fig. 9 Diffuse reflectance UV-visible spectra of (a) TiO_2NTs and Ni_x/TiO_2NTs photoanodes, and (b) $Au_y/Ni_{20}/TiO_2$NTs photoanodes. Tauc plot of (c) Ni_x/TiO_2NTs and (d) $Au_y/Ni_{20}/TiO_2$NTs.

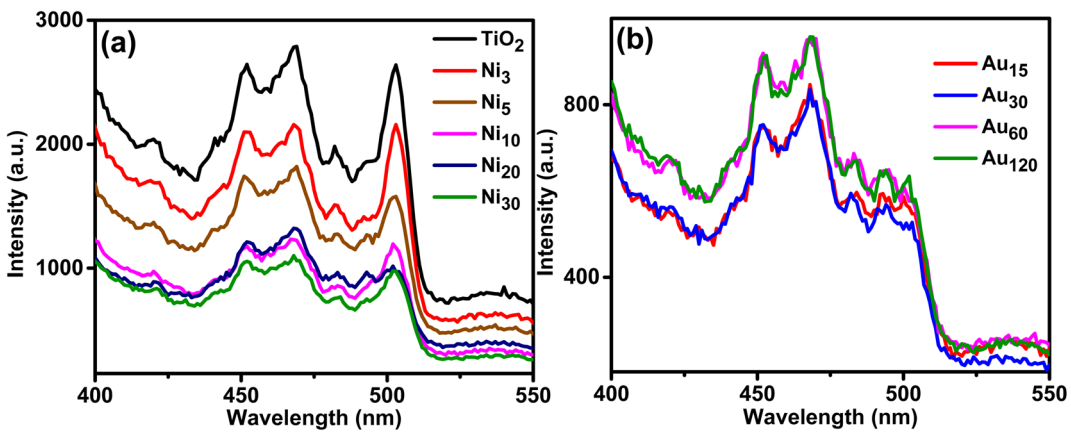

Fig. 10 PL spectra of (a) TiO_2NTs and Ni_x/TiO_2NTs photoanodes, and (b) $Au_y/Ni_{20}/TiO_2$NTs photoanodes.

increase in the photocurrent density was dependent on the number of electrodeposition cycles during preparation and was found in the order Ni_3/TiO_2NTs < Ni_5/TiO_2NTs < Ni_{10}/TiO_2NTs < Ni_{20}/TiO_2NTs ≈ Ni_{30}/TiO_2NTs. The photocurrent density of Ni_{20}/TiO_2NTs was 0.14 mA cm^{-2} that is 1.75-fold of pristine TiO_2NTs, and it can be concluded that 20 cycles of electrodeposition was efficient in producing significant enhancement in the photoanode performance. Photodeposition of gold nanoparticles boosted the OER activity of Ni_{20}/TiO_2NTs photoanode as can be seen in Fig. 11b which revealed the photocurrent density of $Au_y/Ni_{20}/TiO_2$NTs photoanodes was higher than both pristine TiO_2NTs and Ni_{20}/TiO_2NTs due to synergistic effect of co-doping of Ni and Au. The photocurrent densities were found in the order $Au_{120}/Ni_{20}/TiO_2$NTs < $Au_{60}/Ni_{20}/TiO_2$NTs < $Au_{15}/Ni_{20}/TiO_2$NTs < $Au_{30}/Ni_{20}/TiO_2$NTs. The photocurrent density of $Au_{30}/Ni_{20}/TiO_2$NTs was 0.26 mA cm^{-2} that is

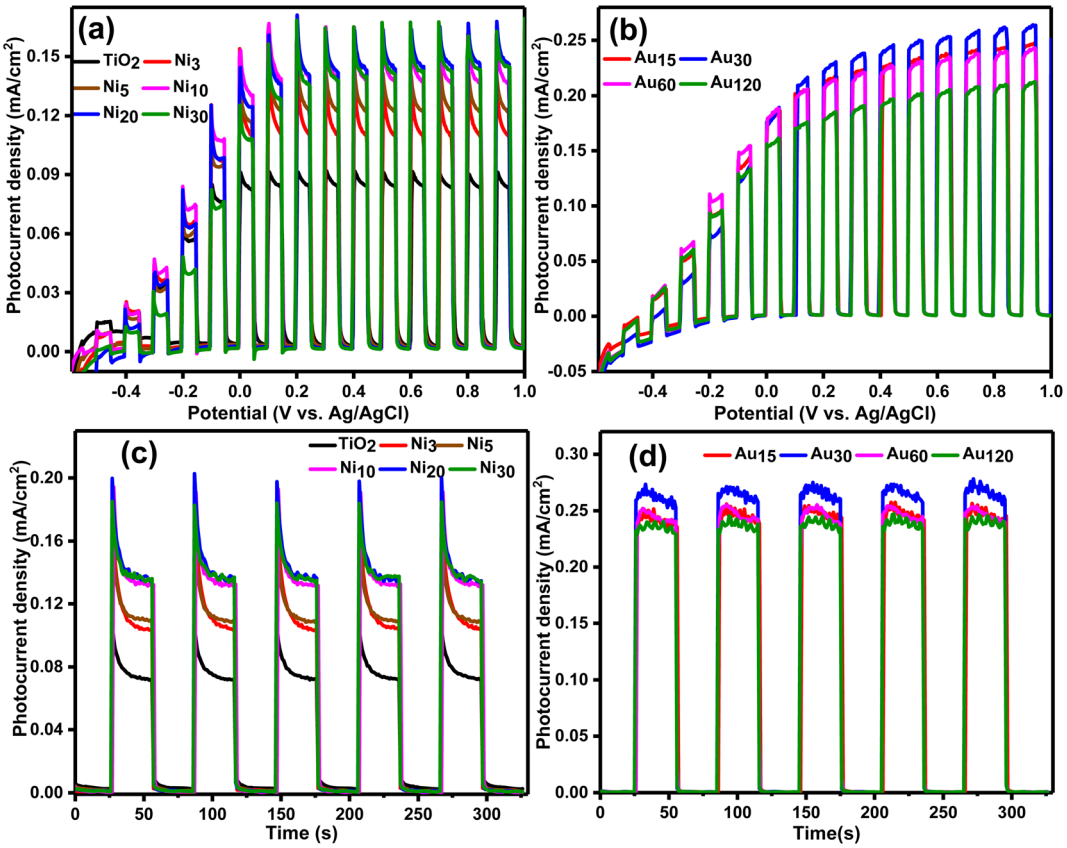

Fig. 11 (LSV) curves at a scan rate of 10 mV for (a) TiO_2NTs and Ni_x/TiO_2NTs photoanodes, and (b) $Au_y/Ni_{20}/TiO_2$NTs photoanodes. The chopped light chronoamperometric measurements at a scan rate of 10 mV for (c) TiO_2NTs and Ni_x/TiO_2NTs photoanodes, and (d) $Au_y/Ni_{20}/TiO_2$NTs photoanodes.

3.25-fold of pristine TiO_2NTs, this enhancement of performance can be explained in light of (PL) results where $Au_{30}/Ni_{20}/TiO_2$-NTs was the most efficient photoanode in charge separation thus suppressing recombination of photogenerated charge carrier which led to enhanced photoelectrochemical performance.

Chronoamperometric measurements measured at 1 V *vs.* Ag/AgCl on the prepared photoanodes under chopped light irradiation was presented in Fig. 11. All the prepared photoanodes showed excellent solar light response as illustrated by the fast photo-response in the ON/OFF cycles and the good reproducibility. The measured photocurrent density of TiO_2NTs was 0.07 mA cm^{-2} which is comparable with published data on TiO_2 photoanodes.[67] Photoanodic current spikes can be observed for TiO_2NTs and Ni_x/TiO_2NTs photoanodes (Fig. 11c) at the onset of the potential attributed to the undesired fast recombination of photo-generated carriers at photoanode surface which limit their transport to the electrolyte. In this situation charge recombination is kinetically faster than charge transport (electrons to bulk regions or holes to the electrolyte).[65] The measured photocurrent density of the prepared Ni_x/TiO_2NTs photoanodes was comparable with the data from LSV showing the same dependence on the number of electrodeposition cycles. Upon photoelectrodepostion of gold on Ni_{20}/TiO_2NTs, the photoanodic current spikes disappeared confirming efficient charge separation. The highest photocurrent density of $Au_y/Ni_{20}/TiO_2$-NTs photoanodes was exhibited by $Au_{30}/Ni_{20}/TiO_2$NTs (0.26 mA cm^{-2}) consistent with LSV measurements. The measured values of photocurrent density were dependant on the number of gold photo-electrodeposition cycle reaching a maximum at 30 cycles. Increase the number of cycles above that limit would cause a slight reduction in the photocurrent density probably due to creation of additional recombination sites.[67] The observed enhanced OER activity of $Au_{30}/Ni_{20}/TiO_2$NTs could be attributed to LSPR effect of nanometric gold which increased solar light harvesting and the synergism between Ni and Au which led to better charge separation and transportation. The obtained data of chronoamperometry was in accordance with the data obtained from optical measurements and linear sweep voltammetry.

Electrochemical impedance spectroscopy was conducted to elucidate the charge transfer characteristics at the photoelectrode/electrolyte interface and the Nyquist plots are given in Fig. 12. It is well known that the radius of semicircle denotes the electron transfer at interface,[68] where a larger radius generally indicates larger electron transfer resistance and lower charge separation efficiency.[58,69,70] As shown in Fig. 12a, the semicircle radius of all Ni_x/TiO_2NTs photoanodes was smaller than that of TiO_2NTs indicating lower charge transfer resistance, long charges lifetime and higher charge separation

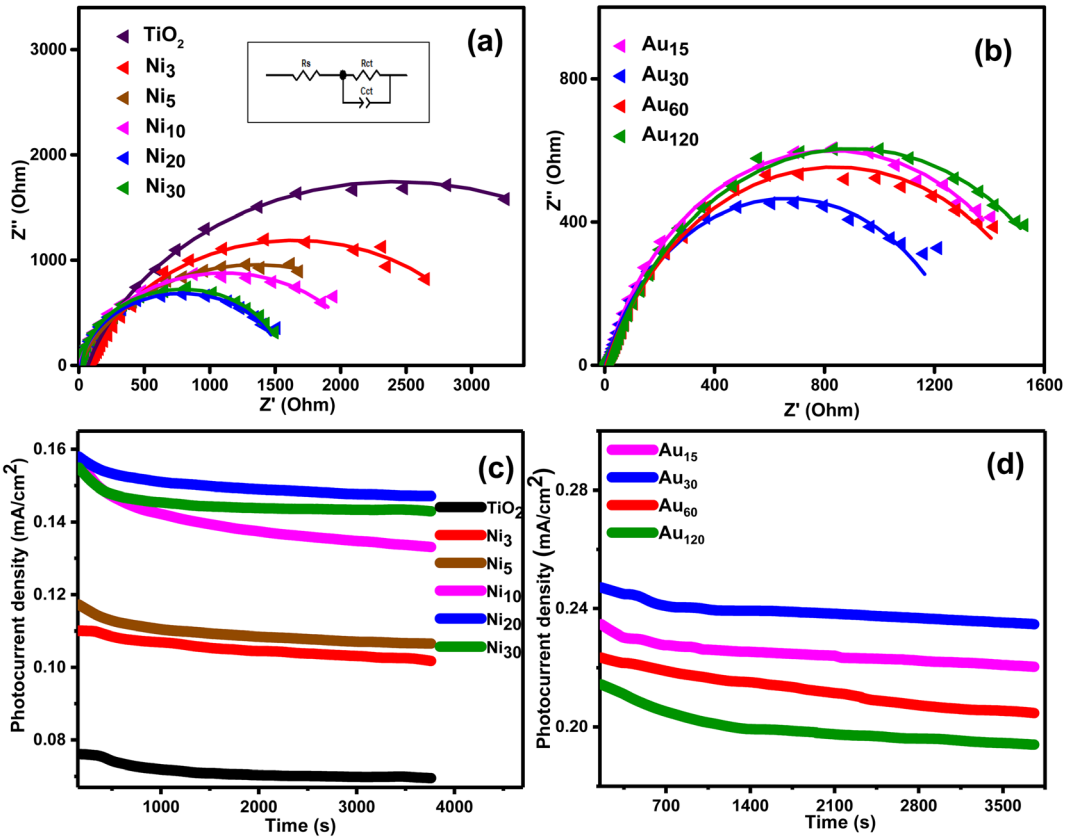

Fig. 12 Electrochemical impedance spectroscopy plot of (a) TiO_2NTs and Ni_x/TiO_2NTs photoanodes, and (b) $Au_y/Ni_{20}/TiO_2$NTs photoanodes. The proposed equivalent circuit (inset (a)). The stability measurement at 1.0 V for 1 h of (c) TiO_2NTs and Ni_x/TiO_2NTs photoanodes, and (d) $Au_y/Ni_{20}/TiO_2$NTs photoanodes.

efficiency.[71] Further reduction in the semicircle radius was observed in $Au_y/Ni_{20}/TiO_2$NTs photoanodes (Fig. 12b) and $Au_{30}/Ni_{20}/TiO_2$NTs showed the smallest charge transport resistance. The equivalent circuit diagram was suggested (inset Fig. 13a) and the values of the charge transfer resistance R_{ct} were calculated. The R_{ct} of pristine TiO_2NTs was 4.80 kΩ which was reduced in Ni_x/TiO_2NTs photoanodes following the order Ni_{20}/TiO_2NTs (1.54 kΩ) < Ni_{30}/TiO_2NTs (1.58 kΩ) < Ni_{10}/TiO_2NTs (2.19 kΩ) < Ni_5/TiO_2NTs (2.54 kΩ) < Ni_3/TiO_2NTs (3.14 kΩ). The values of R_{ct} of $Au_y/Ni_{20}/TiO_2$NTs photoanodes were $Au_{30}/Ni_{20}/TiO_2$NTs (1.34 kΩ) < $Au_{15}/Ni_{20}/TiO_2$NTs (1.65 kΩ) < $Au_{60}/Ni_{20}/TiO_2$NTs (1.67 kΩ) < $Au_{120}/Ni_{20}/TiO_2$NTs (1.75 kΩ). The reduction in R_{ct} values means more holes are participating in water oxidation reaction and better separation efficiency. The photoanode $Au_{30}/Ni_{20}/TiO_2$NTs exhibited the smallest charge transfer resistance and higher charge separation efficiency in accordance with other electrochemical and optical measurement suggesting its application as efficient photoanode in PEC water splitting for H_2 production.

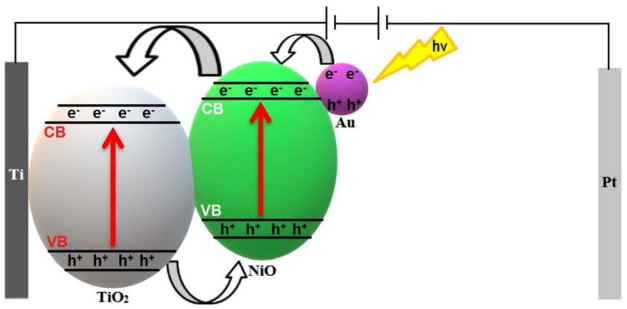

Fig. 13 The proposed mechanism for charge transfer in $Au_y/Ni_{20}/TiO_2$NTs photoanodes during PEC.

The stability of the different photoanodes was determined by chronoamperometry at 1 V *vs.* Ag/AgCl under constant light irradiation and the results obtained during the first hour are shown in Fig. 12. The photocurrent density was marginally reduced for all photoanodes suggesting good stability. Comparison with other reported photoanodes (Table 2) suggested reasonably high photocurrent density of the prepared photoanode which confirmed its potential application as efficient and stable photoanode in PEC water splitting for H_2 production.

The following mechanisms were proposed based on the obtained results from optical and electrochemical measurements after considering the published mechanisms in literature.[1,4,10,14,56,72–74] First for Ni_x/TiO_2NTs photoanodes; a p–n heterojunction was formed across the TiO_2NTs (n-type semiconductor)/NiO (p-type semiconductor) interface. Upon visible light excitation charge carriers were photogenerated in

Table 2 Photocurrent density comparison with other reported photoanodes

Photoanode	Electrolyte	Voltage	Photocurrent density (mA cm^{-2})	Ref.
Ag–N, S–C/TiO_2@CC	0.5 M phosphate buffer solution	1.23 V *vs.* RHE	0.089	75
m-RGO/TiO_{2-x}	0.1 M Na_2SO_4	0.2 V *vs.* SCE	0.018	76
CdSe/TiO_2 NTs	0.2 M Na_2S	0.5 V *vs.* SCE	0.167	77
$AgVO_3$/V_2O_5–TiO_2	0.2 M Na_2SO_3 and 0.1 M Na_2S		0.115	78
GQDs/TiO_2-20	0.5 M Na_2SO_4	0.5 V *vs.* SCE	0.072	79
Cr–S-codoped TiO_2	1.0 M KOH	0.40 V *vs.* Ag/AgCl	0.202	80
TNT-15$Ti_3C_2T_x$	0.5 M Na_2SO_4	0.6 V *vs.* Ag/AgCl	0.177	81
5 nm Au NPs@TNAs	1 M KOH	1.23 V *vs.* RHE	0.140	37
Au(556)/TiO_2NTPC	—	1.23 V *vs.* RHE	0.150	82
W-h-TiO_2	0.1 M Na_2SO_4	0.6 V *vs.* Ag/AgCl	0.080	16
Ni ALD/black TiO_2	1 M KOH	0.23 V *vs.* Ag/AgCl	0.165	26
Ni–TiO_2 nanorods	0.1 M Na_2SO_4	0 V *vs.* (Ag/AgCl)	0.140	66
CFTS/Ni–TiO_2	0.1 M Na_2SO_4	0 V *vs.* (Ag/AgCl)	0.190	66
Au_{30}/Ni_{20}/TiO_2NTs	0.5 M Na_2SO_4	1 V *vs.* Ag/AgCl	0.260	Current work

both semiconductors followed by migration of electrons from the CB of NiO to the CB of TiO_2 then through the electric circle to the Pt wire. Meanwhile the photogenerated holes travelled through the p–n heterojunction interface from TiO_2 VB to NiO VB thus establishing efficient charge separation. The holes in NiO VB directly engaged in H_2O oxidation reaction to produce O_2 gas while H_2 is produced at the Pt cathode. Second for Au_y/Ni_{20}/TiO_2NTs photoanodes (Fig. 13); it was proposed that Au nanoparticles were photo-deposited on the surface of NiO forming Schottky barrier at the Au/NiO interface. Visible light excitation activated the (LSPR) effect which led to enhanced light harvesting and hot electron generation in the plasmonic Au nanoparticles. The hot electrons overcome the Schottky barrier and migrated to the CB of NiO then through the p–n heterojunction interface to the CB of TiO_2 where it was transferred to the cathode. Accordingly, further improvement in the charge separation efficiency and higher photocurrent densities were obtained due to the favorable synergism between the p–n heterojunction and LSPR effects.

4. Conclusion

A series of Ni_x/TiO_2NTs and Au_y/Ni_x/TiO_2NTs photoanodes were prepared and its activity toward photoelectrochemical water-splitting for H_2 production under simulated solar light was investigated. A correlation was found between the photoanodes performance and the number of electrodeposition cycles and duration of photoreduction of gold. The photocurrent density was increased in the order Ni_3/TiO_2NTs < Ni_5/TiO_2NTs < Ni_{10}/TiO_2NTs < Ni_{20}/TiO_2NTs ≈ Ni_{30}/TiO_2NTs. The photocurrent density of Ni_{20}/TiO_2NTs was 0.14 mA cm^{-2} that is 1.75-fold of pristine TiO_2NTs. Photodeposition of gold further boosted the OER activity of Ni_{20}/TiO_2NTs photoanode and was found to increase in the order Au_{120}/Ni_{20}/TiO_2NTs < Au_{60}/Ni_{20}/TiO_2NTs < Au_{15}/Ni_{20}/TiO_2NTs < Au_{30}/Ni_{20}/TiO_2NTs. The photocurrent density of Au_{30}/Ni_{20}/TiO_2NTs was 0.26 mA cm^{-2} that is 3.25-fold of pristine TiO_2NTs, this enhancement was attributed to LSPR effect of nanometric gold and the synergism between Ni and Au leading to better solar light harvesting, charge separation and transportation. This research may have significant implications for the synthesis of nanomaterials with improved light harvesting for photo- and photoelectrocatalytic applications in the future.

Conflicts of interest

There are no conflicts to declare.

References

1 M. A. Marwat, *et al.*, Advanced catalysts for photoelectrochemical water splitting, *ACS Appl. Energy Mater.*, 2021, **4**(11), 12007–12031.
2 F. Zhang and Q. Wang, Redox-mediated water splitting for decoupled H2 production, *ACS Mater. Lett.*, 2021, **3**(5), 641–651.
3 S. Dutta, Review on solar hydrogen: Its prospects and limitations, *Energy Fuels*, 2021, **35**(15), 11613–11639.
4 A. Govind Rajan, J. M. P. Martirez and E. A. Carter, Why do we use the materials and operating conditions we use for heterogeneous (photo) electrochemical water splitting?, *ACS Catal.*, 2020, **10**(19), 11177–11234.
5 S. Jin, What else can photoelectrochemical solar energy conversion do besides water splitting and CO2 reduction?, *ACS Energy Lett.*, 2018, **3**(10), 2610–2612.
6 P. Varadhan, *et al.*, An efficient and stable photoelectrochemical system with 9% solar-to-hydrogen conversion efficiency via InGaP/GaAs double junction, *Nat. Commun.*, 2019, **10**(1), 1–9.
7 L. Deng, *et al.*, MXene decorated by phosphorus-doped TiO2 for photo-enhanced electrocatalytic hydrogen evolution reaction, *Renewable Energy*, 2021, **170**, 858–865.
8 B. Chang, *et al.*, Photo-enhanced electrocatalysis of sea-urchin shaped Ni 3 (VO 4) 2 for the hydrogen evolution reaction, *J. Mater. Chem. A*, 2017, **5**(34), 18038–18043.
9 B. Chang, *et al.*, p–n tungsten oxide homojunctions for Vis-NIR light-enhanced electrocatalytic hydrogen evolution, *J. Mater. Chem. A*, 2019, **7**(33), 19573–19580.

10 C. Ding, *et al.*, Photoelectrocatalytic water splitting: significance of cocatalysts, electrolyte, and interfaces, *ACS Catal.*, 2017, **7**(1), 675–688.
11 X.-C. Lu, *et al.*, Efficient photoelectrodes based on two-dimensional transition metal dichalcogenides heterostructures: from design to construction, *Rare Met.*, 2022, 1–18.
12 M. S. Afify, *et al.*, Effects of Ag doping on LaMnO3 photocatalysts for photoelectrochemical water splitting, *Appl. Phys. A: Mater. Sci. Process.*, 2022, **128**(10), 1–12.
13 S. Zhang, *et al.*, Crystallographic orientation and morphology control of Sb2Se3 to sensitize TiO2 nanotube arrays for enhanced photoelectrochemical performances, *Chem. Eng. J.*, 2022, **429**, 132091.
14 K. Arifin, *et al.*, Improvement of TiO2 nanotubes for photoelectrochemical water splitting, *Int. J. Hydrogen Energy*, 2021, **46**(7), 4998–5024.
15 Q. Guo, *et al.*, Fundamentals of TiO2 photocatalysis: concepts, mechanisms, and challenges, *Adv. Mater.*, 2019, **31**(50), 1901997.
16 X. Chen, *et al.*, Ultrathin tungsten-doped hydrogenated titanium dioxide nanosheets for solar-driven hydrogen evolution, *Inorg. Chem. Front.*, 2022, **9**(17), 4470–4477.
17 J. W. Yoon, *et al.*, Heterojunction between bimetallic metal-organic framework and TiO2: Band-structure engineering for effective photoelectrochemical water splitting, *Nano Res.*, 2022, 1–8.
18 A. E. A. Aboubakr, *et al.*, Effect of morphology and non-metal doping (P and S) on the activity of graphitic carbon nitride toward photoelectrochemical water oxidation, *Sol. Energy Mater. Sol. Cells*, 2021, **232**, 111326.
19 M.-Z. Ge, *et al.*, In situ plasmonic Ag nanoparticle anchored TiO 2 nanotube arrays as visible-light-driven photocatalysts for enhanced water splitting, *Nanoscale*, 2016, **8**(9), 5226–5234.
20 W. M. El Rouby, *et al.*, Surface sensitization of TiO2 nanorod mats by electrodeposition of ZIF-67 for water photo-oxidation, *Electrochim. Acta*, 2020, **339**, 135882.
21 W. M. El Rouby, *et al.*, Role of photosensitizers in enhancing the performance of nanocrystalline TiO2 for photoelectrochemical water splitting, *Nanoscience*, 2021, 181–212.
22 W. Fang, M. Xing and J. Zhang, A new approach to prepare Ti3+ self-doped TiO2 via NaBH4 reduction and hydrochloric acid treatment, *Appl. Catal., B*, 2014, **160**, 240–246.
23 J. Li, *et al.*, Vacancy-enabled mesoporous TiO2 modulated by nickel doping with enhanced photocatalytic nitrogen fixation performance, *ACS Sustainable Chem. Eng.*, 2020, **8**(49), 18258–18265.
24 M. H. Elbakkay, *et al.*, Highly active atomic Cu catalyst anchored on superlattice CoFe layered double hydroxide for efficient oxygen evolution electrocatalysis, *Int. J. Hydrogen Energy*, 2022, **47**(17), 9876–9894.
25 Q. Liu, *et al.*, Black Ni-doped TiO2 photoanodes for high-efficiency photoelectrochemical water-splitting, *Int. J. Hydrogen Energy*, 2015, **40**(5), 2107–2114.
26 C.-C. Wang, *et al.*, Deposition of Ni nanoparticles on black TiO2 nanowire arrays for photoelectrochemical water splitting by atomic layer deposition, *Electrochim. Acta*, 2018, **284**, 211–219.
27 L. Yu, *et al.*, Effect of unsaturated coordination on photoelectrochemical properties of Ni-MOF/TiO2 photoanode for water splitting, *Int. J. Hydrogen Energy*, 2021, **46**(34), 17741–17750.
28 Z. Dong, *et al.*, Facile preparation of Ti3+/Ni co-doped TiO2 nanotubes photoanode for efficient photoelectrochemical water splitting, *Appl. Surf. Sci.*, 2019, **480**, 219–228.
29 S. Fang, Z. Sun and Y. H. Hu, Insights into the thermo-photo catalytic production of hydrogen from water on a low-cost NiO x-loaded TiO2 catalyst, *ACS Catal.*, 2019, **9**(6), 5047–5056.
30 Z. Dong, *et al.*, Ni-doped TiO2 nanotubes photoanode for enhanced photoelectrochemical water splitting, *Appl. Surf. Sci.*, 2018, **443**, 321–328.
31 W.-T. Chen, *et al.*, Performance comparison of Ni/TiO2 and Au/TiO2 photocatalysts for H2 production in different alcohol-water mixtures, *J. Catal.*, 2018, **367**, 27–42.
32 T. Elysabeth, *et al.*, Synthesis of Ni-and N-doped titania nanotube arrays for photocatalytic hydrogen production from glycerol–water solutions, *Catalysts*, 2020, **10**(11), 1234.
33 J. Li, *et al.*, The high surface energy of NiO {110} facets incorporated into TiO2 hollow microspheres by etching Ti plate for enhanced photocatalytic and photoelectrochemical activity, *Appl. Surf. Sci.*, 2017, **396**, 1539–1545.
34 W. Hong, *et al.*, High-performance silicon photoanode enhanced by gold nanoparticles for efficient water oxidation, *ACS Appl. Mater. Interfaces*, 2018, **10**(7), 6262–6268.
35 S. Oros-Ruiz, *et al.*, Photocatalytic hydrogen production by Au–MxOy (MAg, Cu, Ni) catalysts supported on TiO2, *Catal. Commun.*, 2014, **47**, 1–6.
36 Z. Lian, *et al.*, Plasmonic silver quantum dots coupled with hierarchical TiO2 nanotube arrays photoelectrodes for efficient visible-light photoelectrocatalytic hydrogen evolution, *Sci. Rep.*, 2015, **5**(1), 1–10.
37 S. Y. Moon, *et al.*, Plasmonic hot carrier-driven oxygen evolution reaction on Au nanoparticles/TiO 2 nanotube arrays, *Nanoscale*, 2018, **10**(47), 22180–22188.
38 Q. Wang, *et al.*, MoS2 Quantum Dots@ TiO2 Nanotube Arrays: An Extended-Spectrum-Driven Photocatalyst for Solar Hydrogen Evolution, *ChemSusChem*, 2018, **11**(10), 1708–1721.
39 W. Li and T. Zeng, Preparation of TiO2 anatase nanocrystals by TiCl4 hydrolysis with additive H2SO4, *PLoS One*, 2011, **6**(6), e21082.
40 W. Wong-Ng, *et al.*, JCPDS-ICDD research associateship (cooperative program with NBS/NIST), *J. Res. Natl. Inst. Stand. Technol.*, 2001, **106**(6), 1013.
41 L. Barrientos, *et al.*, Unveiling the structure of Ni/Ni oxide nanoparticles system, *J. Chil. Chem. Soc.*, 2009, **54**(4), 391–393.

42 S.-M. You, *et al.*, Fe/Ni Bimetallic Organic Framework Deposited on TiO(2) Nanotube Array for Enhancing Higher and Stable Photoelectrochemical Activity of Oxygen Evaluation Reaction, *Nanomaterials*, 2020, **10**(9), 1688.
43 F. Liao, *et al.*, Carbon dots dominated photoelectric surface in titanium dioxide nanotube/nitrogen-doped carbon dot/gold nanocomposites for improved photoelectrochemical water splitting, *J. Colloid Interface Sci.*, 2022, **606**, 1274–1283.
44 S. Kumbhar, S. Shaikh and K. Rajpure, Hydrothermally-Grown TiO2 thin film-based metal–semiconductor–metal UV photodetector, *J. Electron. Mater.*, 2020, **49**(1), 499–509.
45 R. Yalavarthi, *et al.*, Radiative and non-radiative recombination pathways in mixed-phase TiO2 nanotubes for PEC water-splitting, *Catalysts*, 2019, **9**(2), 204.
46 L. Manuel, *et al.*, One-pot synthesis of Au/N-TiO2 photocatalysts for environmental applications: Enhancement of dyes and NOx photodegradation, *Powder Technol.*, 2019, **355**, 793–807.
47 F. Settle, *Handbook of instrumental techniques for analytical chemistry*, 1997.
48 M. Hinojosa-Reyes, *et al.*, Gold-TiO2-Nickel catalysts for low temperature-driven CO oxidation reaction, *Appl. Surf. Sci.*, 2016, **368**, 224–232.
49 S. K. Khore, *et al.*, Solar light active plasmonic Au@ TiO 2 nanocomposite with superior photocatalytic performance for H 2 production and pollutant degradation, *New J. Chem.*, 2018, **42**(13), 10958–10968.
50 Y. Fu, *et al.*, XPS characterization of surface and interfacial structure of sputtered TiNi films on Si substrate, *Mater. Sci. Eng., A*, 2005, **403**(1–2), 25–31.
51 H. Zhang, *et al.*, Self-powered TiO2 NRs UV photodetectors: Heterojunction with PTTh and enhanced responsivity by Au nanoparticles, *J. Alloys Compd.*, 2022, **899**, 163279.
52 D.-M. Amaya-Dueñas, *et al.*, A-site deficient chromite with in situ Ni exsolution as a fuel electrode for solid oxide cells (SOCs), *J. Mater. Chem. A*, 2021, **9**(9), 5685–5701.
53 S. A. Tenney, *et al.*, Characterization of Pt–Au and Ni–Au Clusters on TiO2 (110), *Top. Catal.*, 2011, **54**(1), 42–55.
54 H. Wang, *et al.*, Effective photocatalytic properties of N doped Titanium dioxide nanotube arrays prepared by anodization, *React. Kinet., Mech. Catal.*, 2012, **106**(2), 341–353.
55 S. Zhang, *et al.*, Electrodeposition preparation of Ag loaded N-doped TiO2 nanotube arrays with enhanced visible light photocatalytic performance, *Catal. Commun.*, 2011, **12**(8), 689–693.
56 E. Fudo, *et al.*, Modification of gold nanoparticles with a hole-transferring cocatalyst: a new strategy for plasmonic water splitting under irradiation of visible light, *Sustainable Energy Fuels*, 2021, **5**(13), 3303–3311.
57 Y. Yu, *et al.*, UV and visible light photocatalytic activity of Au/TiO2 nanoforests with Anatase/Rutile phase junctions and controlled Au locations, *Sci. Rep.*, 2017, **7**(1), 41253.
58 W. M. El Rouby and A. A. Farghali, Titania morphologies modified gold nanoparticles for highly catalytic photoelectrochemical water splitting, *J. Photochem. Photobiol., A*, 2018, **364**, 740–749.
59 S. K. Mohamed, *et al.*, Facile fabrication of ordered mesoporous Bi/Ti-MCM-41 nanocomposites for visible light-driven photocatalytic degradation of methylene blue and CO oxidation, *Sep. Purif. Technol.*, 2018, **195**, 174–183.
60 E. M. Neville, *et al.*, Visible light active C-doped titanate nanotubes prepared via alkaline hydrothermal treatment of C-doped nanoparticulate TiO2: Photo-electrochemical and photocatalytic properties, *J. Photochem. Photobiol., A*, 2013, **267**, 17–24.
61 A. Talla, *et al.*, Effect of annealing temperature and atmosphere on the structural, morphological and luminescent properties of TiO2 nanotubes, *Phys. B*, 2022, 414026.
62 Q. Kang, *et al.*, Reduced TiO 2 nanotube arrays for photoelectrochemical water splitting, *J. Mater. Chem. A*, 2013, **1**(18), 5766–5774.
63 G. Marcì and L. Palmisano, *Heterogeneous photocatalysis: Relationships with heterogeneous catalysis and perspectives*, Elsevier, 2019.
64 L. Lin, *et al.*, Size effect of Au nanoparticles in Au-TiO2-x photocatalyst, *Chem. Phys. Lett.*, 2021, **770**, 138457.
65 C. S. Yaw, *et al.*, A Type II nn staggered orthorhombic V2O5/monoclinic clinobisvanite BiVO4 heterojunction photoanode for photoelectrochemical water oxidation: fabrication, characterisation and experimental validation, *Chem. Eng. J.*, 2019, **364**, 177–185.
66 N. Mukurala, *et al.*, Cu2FeSnS4 decorated Ni-TiO2 nanorods heterostructured photoanode for enhancing water splitting performance, *Appl. Surf. Sci.*, 2021, **551**, 149377.
67 P. Peerakiatkhajohn, *et al.*, Surface plasmon-driven photoelectrochemical water splitting of a Ag/TiO 2 nanoplate photoanode, *RSC Adv.*, 2022, **12**(5), 2652–2661.
68 C. Chen, *et al.*, Morphology-controlled In 2 O 3 nanostructures enhance the performance of photoelectrochemical water oxidation, *Nanoscale*, 2015, **7**(8), 3683–3693.
69 T. Li, *et al.*, Fabrication of n-type CuInS2 modified TiO2 nanotube arrays heterostructure photoelectrode with enhanced photoelectrocatalytic properties, *Appl. Catal., B*, 2014, **156**, 362–370.
70 W. M. El Rouby, *et al.*, Synthesis and characterization of Bi-doped g-C3N4 for photoelectrochemical water oxidation, *Sol. Energy*, 2020, **211**, 478–487.
71 M. Zhang, *et al.*, AgInS2 nanoparticles modified TiO2 nanotube array electrodes: Ultrasonic-assisted SILAR preparation and mechanism of enhanced photoelectrocatalytic activity, *Mol. Catal.*, 2017, **442**, 97–106.
72 S. Huo, *et al.*, Core–shell TiO2@ Au25/TiO2 nanowire arrays photoanode for efficient photoelectrochemical full water splitting, *Ind. Eng. Chem. Res.*, 2020, **59**(32), 14224–14233.
73 X. Shi, *et al.*, Plasmon-enhanced photocurrent generation and water oxidation with a gold nanoisland-loaded titanium dioxide photoelectrode, *J. Phys. Chem. C*, 2013, **117**(6), 2494–2499.
74 N. Celebi, *et al.*, Ligand-free fabrication of Au/TiO2 nanostructures for plasmonic hot-electron-driven

photocatalysis: Photoelectrochemical water splitting and organic-dye degredation, *J. Alloys Compd.*, 2021, **860**, 157908.

75 Y. Zhang, *et al.*, Surface plasmon resonance metal-coupled biomass carbon modified TiO2 nanorods for photoelectrochemical water splitting, *Chin. J. Chem. Eng.*, 2022, **41**, 403–411.

76 S. Wang, *et al.*, Defective black Ti3+ self-doped TiO2 and reduced graphene oxide composite nanoparticles for boosting visible-light driven photocatalytic and photoelectrochemical activity, *Appl. Surf. Sci.*, 2019, **467**, 45–55.

77 W. Wang, *et al.*, Photoelectrocatalytic hydrogen generation and simultaneous degradation of organic pollutant via CdSe/TiO2 nanotube arrays, *Appl. Surf. Sci.*, 2016, **362**, 490–497.

78 H. Yu, *et al.*, Fabrication of a stable light-activated and p/n type AgVO3/V2O5-TiO2 heterojunction for pollutants removal and photoelectrochemical water splitting, *J. Alloys Compd.*, 2022, **894**, 162500.

79 Z. Xiao, *et al.*, Preparation of GQDs/TiO2 nanotube heterojunction photoanode and its photoelectrochemical performance for water splitting, *Int. J. Electrochem. Sci.*, 2022, **17**(220817), 2.

80 M. M. Momeni, *et al.*, Preparation of chromium and sulfur single and co-doped TiO2 nanostructures for efficient photoelectrochemical water splitting: effect of aliphatic alcohols on their activity, *J. Solid State Electrochem.*, 2022, **26**(1), 281–291.

81 N. Khatun, *et al.*, Ti3C2Tx MXene functionalization induced enhancement of photoelectrochemical performance of TiO2 nanotube arrays, *Mater. Chem. Phys.*, 2022, **278**, 125651.

82 Z. Zhang, *et al.*, Plasmonic gold nanocrystals coupled with photonic crystal seamlessly on TiO2 nanotube photoelectrodes for efficient visible light photoelectrochemical water splitting, *Nano Lett.*, 2013, **13**(1), 14–20.